A hot sub-Neptune in the desert and a temperate super-Earth around faint M dwarfs Color validation of TOI-4479b and TOI-2081b

A&A 666, A10 (2022)
https://doi.org/10.1051/0004-6361/202243731

Astronomy & Astrophysics

A hot sub-Neptune in the desert and a temperate super-Earth around faint M dwarfs

Color validation of TOI-4479b and TOI-2081b

E. Esparza-Borges[1,2], H. Parviainen[1,2], F. Murgas[1,2], E. Pallé[1,2], A. Maas[3,4], G. Morello[1,2], M. R. Zapatero-Osorio[5], K. Barkaoui[13,28,1], N. Narita[17,18,1], A. Fukui[17,1], N. Casasayas-Barris[6], M. Oshagh[1,2], N. Crouzet[6], D. Galán[2], G. E. Fernández[1], T. Kagetani[24], K. Kawauchi[1,2], T. Kodama[17], J. Korth[10], N. Kusakabe[18,20], A. Laza-Ramos[1], R. Luque[11], J. Livingston[18,20,19], A. Madrigal-Aguado[1], M. Mori[19], J. Orell-Miquel[1,2], M. Puig-Subirà[1], M. Stangret[1,2], Y. Terada[25,26], N. Watanabe[24], Y. Zou[24], A. Baliga Savel[9], A. A. Belinski[12], K. Collins[7], C. D. Dressing[8], S. Giacalone[8], H. Gill[8], M. V. Goliguzova[12], M. Ikoma[21], J. M. Jenkins[23], M. Tamura[18,19,20], J. D. Twicken[22,23], G. R. Ricker[15,16], R. P. Schwarz[14], S. Seager[15,16,27,28], A. Shporer[15], R. Vanderspek[15,16], and J. Winn[29]

(Affiliations can be found after the references)

Received 7 April 2022 / Accepted 17 June 2022

ABSTRACT

Aims. We report the discovery and validation of two TESS exoplanets orbiting faint M dwarfs: TOI-4479b and TOI-2081b.
Methods. We jointly analyzed space (TESS mission) and ground-based (MuSCAT2, MuSCAT3 and SINISTRO instruments) light curves using our multicolor photometry transit analysis pipeline. This allowed us to compute contamination limits for both candidates and validate them as planet-sized companions.
Results. We found TOI-4479b to be a sub-Neptune-sized planet ($R_p = 2.82^{+0.65}_{-0.63}\ R_\oplus$) and TOI-2081b to be a super-Earth-sized planet ($R_p = 2.04^{+0.50}_{-0.54}\ R_\oplus$). Furthermore, we obtained that TOI-4479b, with a short orbital period of $1.15890^{+0.00002}_{-0.00001}$ days, lies within the Neptune desert and is in fact the largest nearly ultra-short period planet around an M dwarf known to date.
Conclusions. These results make TOI-4479b rare among the currently known exoplanet population of M dwarf stars and an especially interesting target for spectroscopic follow-up and future studies of planet formation and evolution.

Key words. planets and satellites: individual: TOI-4479b – planets and satellites: individual: TOI-2081b – methods: observational – techniques: photometric – planets and satellites: general – planets and satellites: detection

1. Introduction

Since the beginning of its observations in 2018, the Transiting Exoplanet Survey Satellite (TESS, Ricker et al. 2015) has provided nearly 5500 objects of interest and 204 confirmed planets[1]. Although many of these objects of interest may be consistent with a planetary-like transit signal, not all of them have a planetary nature. Several astrophysical objects – such as a brown dwarf or a low-mass star transiting a binary companion, a grazing binary stellar system, or a pair of blended binaries – are able to mimic the signal of a planetary transit. Although these systems would produce deep eclipses, we could be observing their photometry diluted by a bright neighbor star (Cameron 2012; Ciardi et al. 2015). Therefore, the nature of each object of interest needs to be determined by ground-based follow-up observations, which play a supporting role by being able to confirm whether the candidate is a planet or not.

Moreover, although the most reliable method to confirm a planet candidate is the mass determination through radial velocity (RV) measurements, this procedure is very difficult for those candidates orbiting a faint, active, or fast rotating star. Hence, to determine the nature of these candidates it is necessary to use other methods to validate them as planets.

In this context, ground-based multicolor transit photometry is a useful method to validate planet candidates (Drake 2003; Tingley 2004; Parviainen et al. 2019, 2020, 2021; Fukui et al. 2022). It allows us to account for the light contamination from unresolved sources and estimate the uncontaminated radius ratio of the transiting candidate. With an estimate of the stellar radius, combined with the uncontaminated radius ratio, the radius of the candidate can be obtained. Consequently, if the radius of the candidate is significantly below the theoretical radius limit of a brown dwarf, the candidate can be validated as a planet (Parviainen et al. 2020).

Here, we used the approach of Parviainen et al. (2020) to validate the substellar nature of two TESS objects of interest orbiting faint ($V = 13.369$ mag and $V = 15.180$ mag) M dwarfs: the super-Earth-sized TOI-2081b and the sub-Neptune-sized TOI-4479b. We find TOI-4479b to be a rare target that lies on the Neptune desert.

Our analysis is performed over space-based TESS photometry, ground-based datasets of multicolor photometry in the g, r, i, and z_s bands obtained through MuSCAT2 and MuSCAT3 multicolor imagers, and complementary ground-based

[1] From the `NASA Exoplanet Archive`.

single-passband photometry from the SINISTRO camera. We also obtained low-resolution optical spectra for the stellar characterization. In addition, high angular resolution observations are used to visually discard a binary stellar companion.

In Sects. 2 and 3, we describe the observations used in our study. In Sect. 5, we explain the methodology followed for the light-curve analysis and the validation procedure. In Sect. 6, we present and discuss our results, which confirm the planetary nature of TOI-2081b and TOI-4479b. Finally, we conclude our study in Sect. 7.

2. TESS photometry

TOI-4479 (TIC 126606859) was observed with two-minute cadence by TESS (Ricker et al. 2015) in Sector 41 over 29 days (from UTC 2021 July 23 to UTC 2021 August 20) during Cycle 4, obtaining 22 full transits in total. Full frame image (FFI) observations are also available in Sector 15, but they have not been used here. In this case, a transit signal with a 1.159 day orbital period and $S/N = 9.5$ was identified in the TESS Science Processing Operations Center (SPOC, Jenkins et al. 2016) transiting planet search (Jenkins 2002; Jenkins et al. 2010, 2020) of the two-minute data from Sector 41. The threshold crossing event was promoted to TESS Object of Interest (TOI) planet candidate status and designated TOI 4479.01 (Guerrero et al. 2021) based on a SPOC data validation report (Twicken et al. 2018; Li et al. 2019) showing clean transiting planet model fit and diagnostic test results.

TOI-2081 (TIC 321669174) was observed by TESS with two-minute cadence in Sectors 14, 17, 20, 21, 24, 25, 26, 40, 41, and 47 (a total duration of 196 days during Cycle 2 and 59 days during Cycle 4), obtaining 22 full transits in total. A transit signal with a 10.504 day orbital period and $S/N = 9.0$ was identified in the TESS SPOC of the combined two-minute data from Sectors 14, 17, 20, and 21. The threshold crossing event was promoted to TOI planet candidate status and designated TOI 2081.01.

The TESS images around the position of TOI-4479 and TOI-2081 in Sector 41 are shown in Fig. 1. The TESS images in the rest of sectors where TOI-2081 was observed are shown in Fig. A.1.

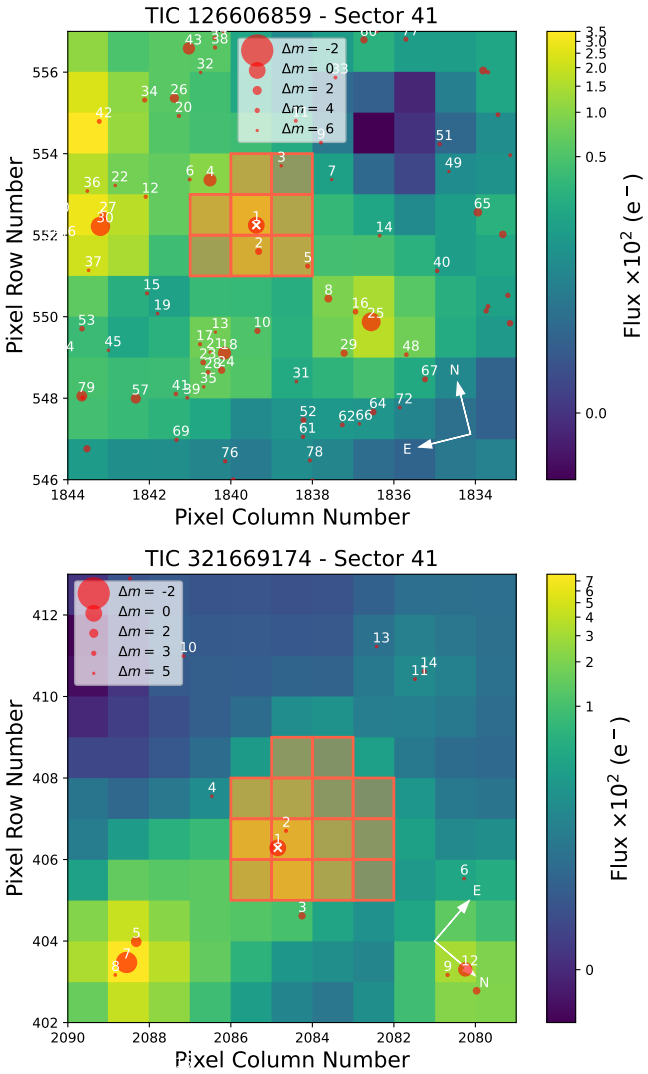

Fig. 1. TESS target pixel file images of TOI-4479 (*top*) and TOI-2081 (*bottom*) observed in Sector 41. The red circles show the sources in the field identified by the *Gaia* DR2 catalogue (Gaia Collaboration 2018) with scaled magnitudes. The position of the targets are indicated by white crosses and the mosaic of orange squares show the mask used by the pipeline to extract photometry. These plots were made using `tpfplotter` (Aller et al. 2020).

3. Ground-based follow-up observations

3.1. MuSCAT2 photometry

We observed a full transit of TOI-4479b on UTC 2021 October 17 and a full transit of TOI-2081b on UTC 2020 July 22 with the MuSCAT2 instrument (Narita et al. 2019) mounted on the Telescopio Carlos Sánchez (TCS) at the Teide Observatory, Spain. MuSCAT2 is a multicolor imager capable of performing simultaneous photometry in the g, r, i, and z_s photometric bands using four independent CCDs. The exposure times used for TOI-4479 and TOI-2081 observations were set independently for each CCD (g, r, i, z_s): (15, 30, 25, 20) and (10, 25, 25, 15) s, respectively. As the objects are red, the exposure times were shorter in redder filters to avoid saturation. The g filter is an exception; since the flux there is small, we set a short integration time and used this channel's images to auto-guide the instrument, for which we want an exposure time typically <15s.

A dedicated MuSCAT2 pipeline, described by Parviainen et al. (2020), was used to perform the data reduction and to extract the photometry. The pipeline performs aperture photometry for a set of comparison stars and aperture sizes (see Fig. 2). The final relative light curves are obtained through the global optimization of a model, which aims to find the optimal comparison stars and aperture sizes, while the transit and baseline variations are simultaneously modeled using a linear combination of covariates.

3.2. MuSCAT3 photometry

A full transit of TOI-4479b was observed simultaneously in Sloan g, r, i, and Pan-STARRS z-short bands on UTC 2021 October 21 using the Las Cumbres Observatory Global Telescope (LCOGT; Brown et al. 2013) 2 m Faulkes Telescope North at Haleakala Observatory on Maui, Hawai'i. The telescope is equipped with the MuSCAT3 multiband imager (Narita et al. 2020). We used the `TESS Transit Finder` to schedule our transit observations. The images were calibrated using the standard LCOGT BANZAI pipeline, and the differential photometric data were extracted in each band using `AstroImageJ` (Collins et al. 2017) with circular apertures with a radius of 2.″7. The

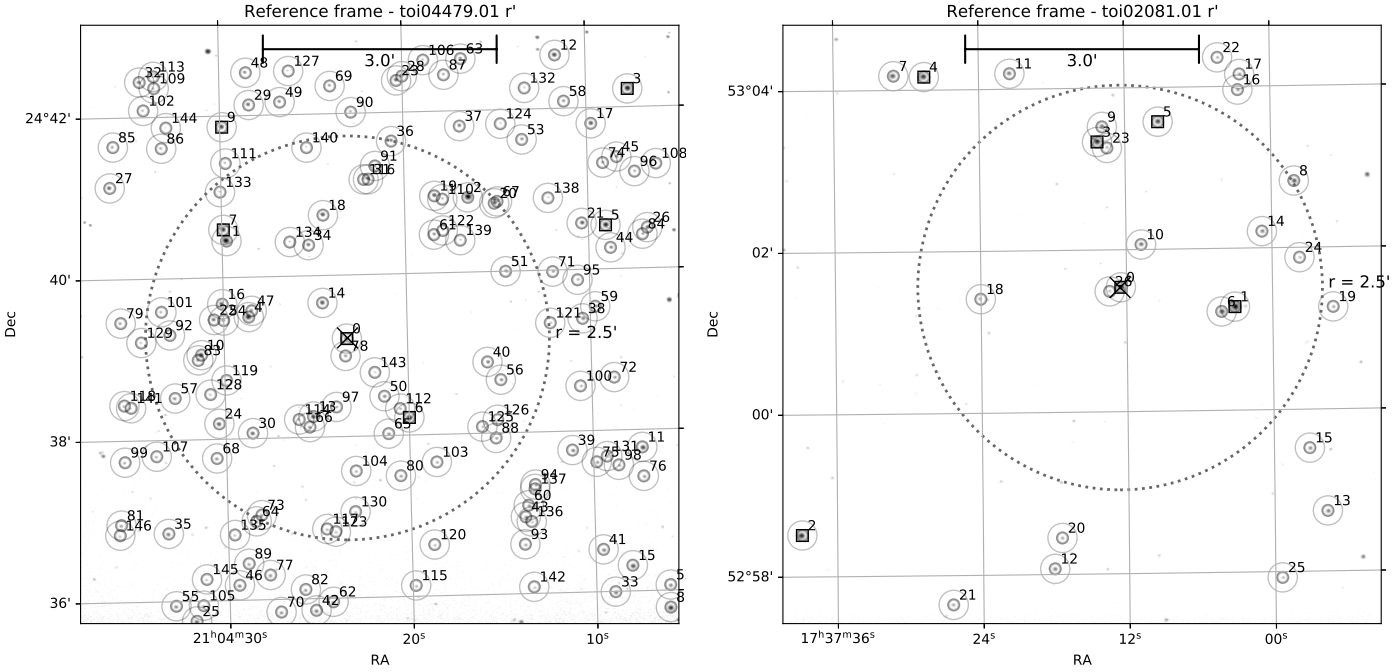

Fig. 2. MuSCAT2 field in the r band during the TOI-4479 (*left*) and TOI-2081 (*right*) observations. The cross indicates the position of the target, and the dotted circle marks the 2.5′-radius region centered around it.

apertures exclude virtually all of the flux from the nearest *Gaia* EDR3 (Gaia Collaboration 2021) neighbor (TIC 1951208113) 8.″7 east of the target. The transit was detected on-target in all four filter bands.

3.3. LCOGT 1 m photometry

We observed a full transit of TOI-4479b from the Las Cumbres Observatory Global Telescope LCOGT 1.0 m network on UTC 2021 October 11 in Sloan i' band. We used the `TESS Transit Finder` (Jensen 2013) to schedule our transit observations. The 1 m telescopes are equipped with 4096 × 4096 SINISTRO cameras having an image scale of 0.″389 per pixel, resulting in a 26′ × 26′ field of view. The images were calibrated by the standard LCOGT `BANZAI` pipeline (McCully et al. 2018). The differential photometric data were extracted using `AstroImageJ` (Collins et al. 2017) with circular photometric apertures having radius 4.″7. The target star aperture excludes most of the flux of the nearest *Gaia* EDR3 and TESS Input Catalog neighbor (TIC 1951208113) 8.″7 east of the target. The transit was detected on-target.

3.4. High-resolution imaging of TOI-2081

We observed TOI-2081 on UTC 2021 March 29 using the ShARCS camera on the Shane 3-meter telescope at the Lick Observatory (Kupke et al. 2012; Gavel et al. 2014; McGurk et al. 2014). Observations were taken with the Shane adaptive optics system in natural guide star mode in order to search for nearby, unresolved stellar companions. We collected one sequence of observations using a Ks filter (λ_0 = 2.150 µm, $\Delta\lambda$ = 0.320 µm) and reduced the data using the publicly available `SImMER` pipeline (Savel et al. 2020)[2]. Our reduced images and corresponding contrast curves are shown in the top panel of Fig. 3. We find no nearby stellar companions within our detection limits.

[2] https://github.com/arjunsavel/SImMER

We also observed TOI-2081 on UTC 2021 March 03 with the Speckle Polarimeter (SPP, Safonov et al. 2017) on the 2.5 m telescope at the Caucasian Observatory of the Sternberg Astronomical Institute (SAI) of Lomonosov Moscow State University. SPP uses the electron multiplying CCD Andor iXon 897 as a detector. The atmospheric dispersion compensator allowed observations of this relatively faint target through the wide-band I_c filter. The power spectrum was estimated from 4000 frames with 30 ms exposure. The detector has a pixel scale of 20.6 mas pixel^{-1}, and the angular resolution was 89 mas. We did not detect any stellar companions brighter than ΔI_C = 2.4 and 3.1 at ρ = 0.″25 and 1.″0, respectively, where ρ is the separation between the source and the potential companion.

Nearby faint companions of the host star may remain undetected through seeing-limited photometry, but could contribute to a contamination of the flux of the target and lead to incorrect estimations of the planetary radius. However, the Shane-AO and SAI-Speckle (Fig. 3) observations allow us to rule out this scenario for TOI-2081 in the K_s and I bands. We do not detect any nearby visual companion, and TOI-2081 seems to be an isolated star in the data.

3.5. ALFOSC spectroscopy

TOI-2081 and TOI-4479 were spectroscopically observed with the Alhambra Faint Object Spectrograph and Camera (ALFOSC), mounted on the Cassegrain focus of the 2.5-m Nordic Optical Telescope (NOT) on the Observatorio del Roque de los Muchachos (La Palma, Spain), on 2022 April 8 and 10 UT, respectively. ALFOSC is equipped with a monolithic 2048 × 2048 E2V detector that has a pixel size of 0.″2138 on the sky. On both nights, we used a long slit with a slit width of 1.″0 and the grating number 5. This instrumental configuration yields low-resolution spectra covering the optical wavelength interval from 500 through 1050 nm with a nominal dispersion of 3.38 Å pixel^{-1} (or resolving power R = 610 at 725 nm). However, fringing is strong (≥4%) redwards of ≈900 nm; therefore, we

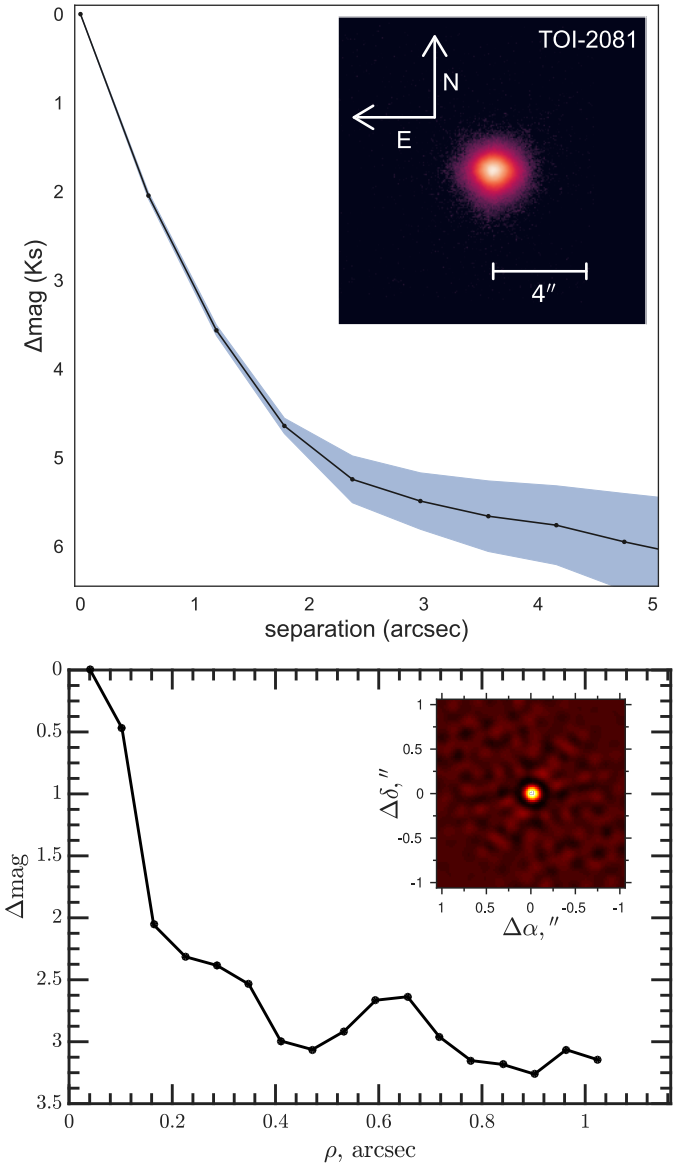

Fig. 3. High-resolution imaging of TOI-2081. *Top*: adaptive optics images of TOI-2081 taken with the ShARCS camera on the Shane 3-meter telescope at the Lick Observatory. For each image, we also present a contrast curve generated by calculating the median values (solid lines) and root-mean-square errors (blue, shaded regions) in annuli centered on each target, where the bin width of each annulus is equal to the full width at half maximum of the point spread function. The observations rule out the presence of a possible nearby contaminant companion. *Bottom*: high angular resolution speckle imaging of TOI-2081 in *I* filter using SAI-2.5 m telescope. The observation rules out the presence of a possible nearby contaminant companion. The structure in this contrast curve is due to the first derivative discontinuity in the frequency mask that is used to compute the autocorrelation. This discontinuity generates rings at characteristic distances from the center, which then have a minor effect on the detection limit.

discarded all data at longer wavelengths. Two exposures of 900 s each were acquired for TOI-2081 and TOI-4479 at an air mass of 1.10 and 1.58, respectively. Together with the main targets, we also observed the spectroscopic standard star BD+26 2606 at different air masses for a proper correction of the instrumental response and telluric absorption. Three exposures of 15 s each were acquired on each night for the stardard star. BD+26 2606 is an early-type star with known fluxes published in Oke (1990).

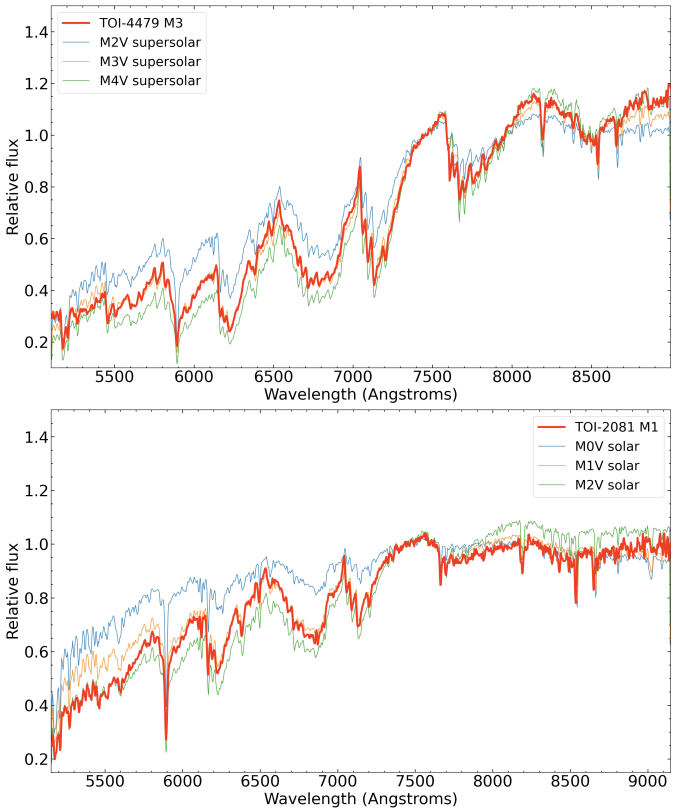

Fig. 4. ALFOSC spectra (red) of TOI-4479 (*top panel*) and TOI-2081 (*bottom panel*) are shown in comparison with solar metallicity templates of known spectral type from the library of Kesseli et al. (2017).

All observations were acquired at a parallactic angle to minimize light losses on the slit. We windowed the ALFOSC detector along the spatial axis (perpendicularly to the dispersion axis) to a size of 500 pixels.

The ALFOSC spectra of the targets and the standard star were reduced and optimally extracted following standard steps within the IRAF environment (Tody 1993). First, we removed the detector bias at the same time we subtracted "the sky" contribution using the region on both sides of the spectral trace of the stars. The spectra were calibrated in wavelength with a precision of about 1.5 Å using observations of He+Ne lamps acquired immediately after observing the main targets. The ALFOSC spectra of TOI-2081 and TOI-4479 were corrected for instrumental response using the observations of the standard star. The final step was to mask out the hydrogen lines intrinsic to the standard star and to normalize its spectra to the continuum for division with the target's spectrum (in this way, we removed the Earth's telluric lines from the spectrum). The telluric-free spectra of TOI-2081 and TOI-4479 are shown in Fig. 4.

4. Stellar parameters

In Fig. 4, the ALFOSC spectra are compared to spectral standard stars from the library of empirical stellar spectra of Kesseli et al. (2017). Our data are characterized by the presence of TiO absorption over the optical wavelengths, which is a signpost of M spectral classification. Using templates of solar metallicity, we derived the following spectral types: M1.0 ± 0.5 (TOI-2081) and M3.0 ± 0.5 (TOI-4479). The ALFOSC spectra are well reproduced by the templates with no significant deviations. Hα is not

Table 1. TOI-4479 and TOI-2081 identifiers, coordinates, magnitudes, and stellar parameters.

Main identifiers	TOI-4479	TOI-2081
TIC	126606859	321669174
2MASS	J21042315+2439153	J17371272+5301326
WISE	J210423.23+243913.8	J173712.60+530132.2
Equatorial coordinates		
RA (J2000)	$21^h04^m23^s.27$	$17^h37^m12^s.54$
Dec (J2000)	$24°39'13''.23$	$53°01'32''.04$
Magnitudes		
TESS	12.9374 ± 0.0075	11.642 ± 0.007
V	15.2 ± 0.2	13.369 ± 0.035
Gaia DR2	14.1309 ± 0.0005	12.6594 ± 0.0003
J	11.44 ± 0.02	10.36 ± 0.02
H	10.85 ± 0.02	9.75 ± 0.03
K	10.65 ± 0.02	9.52 ± 0.02
Stellar parameters[1]		
Spectral type	M3.0 ± 0.5	M1.0 ± 0.5
$M_\star$ [$M_\odot$]	0.452 ± 0.090	0.540 ± 0.080
$R_\star$ [$R_\odot$]	0.451 ± 0.085	0.534 ± 0.080
$L_\star$ [$L_\odot$]	0.02487 ± 0.00015	0.04587 ± 0.00023
log g [dex]	≥4.5	≥4.5
$T_{\rm eff}$ [K]	3400 ± 100	3800 ± 100
[Fe/H] [dex]	≥0.0	≥ − 0.5
Parallax [mas][2]	12.41 ± 0.02	16.05 ± 0.01
Distance [pc][2]	80.6 ± 0.1	62.31 ± 0.05

Notes. [1]Derived from ALFOSC spectroscopy and analysis of the stellar SED. [2] *Gaia* EDR3.

in emission in any of the two dwarfs. Template spectra from Kesseli et al. (2017) are binned by metallicity from −2.0 dex through +1.0 dex, and are separated into main-sequence (dwarf) stars and giant stars. We also compared the ALFOSC data to the sets of different metallicities and gravities, finding that TOI-2081 and TOI-4479 are better described by high-gravity surfaces and atmospheric metallicities of [Fe/H] ≥ −0.5 and ≥0.0 dex, respectively, thus supporting the solar-to-metal-rich nature of both stars. At low resolution, we cannot better constrain the metallicity or surface gravity of the targets.

To derive the stellar mass and radius, we first built the stars' spectral energy distribution (SED) by combining the ALFOSC data and all available broad-band photometry from *Gaia* DR3 (Gaia Collaboration 2021), the JHK magnitudes from 2MASS (Skrutskie et al. 2006), and the $W1 - W4$ magnitudes from *WISE* (Wright et al. 2010). All these data were converted into the absolute fluxes by using the *Gaia* trigonometric distances. The extension of the SEDs toward bluer and redder wavelengths was done with the BT-Settl model (Allard et al. 2012) that best reproduces the observations. The integration of the SEDs yields the bolometric luminosities provided in Table 1. We then employed the bolometric luminosities and the mass–radius–luminosity relations of Cifuentes et al. (2020) to derive the TOI-2081 and TOI-4479 stellar parameters, which are listed in Table 1 and was used in our analysis of the planetary systems.

5. Light-curve analysis

5.1. Multicolor transit analysis

The TESS[3] and ground-based light curves were analyzed individually and jointly following the procedure described in Parviainen et al. (2019, 2020, 2021), which performs an exoplanet-orientated Bayesian parameter estimation (Parviainen 2018). The multicolor analysis procedure can be summarized in the following steps. In the first step a flux model is generated to fit the light curves, accounting for both the transit signal and the systematic effects present in the time series. In the second step a noise model is defined to account for the stochastic variability in the data. In the third step, The likelihood is obtained combining the flux model, the noise model and the observations. Finally, a Markov chain Monte Carlo (MCMC) sampling is performed to obtain the joint parameter posterior distribution based on the priors defined from the model parameters.

The pipeline used to perform the multicolor analysis makes use of `PHOENIX` (Husser et al. 2013) for physics-based contamination modeling; `LDTk` (Parviainen & Aigrain 2015) for limb-darkening estimations; `PyTRANSIT` (Parviainen 2015), which provides flux and noise models; and `emcee` (Foreman-Mackey et al. 2013) to perform the MCMC sampling.

We applied the multicolor analysis to the complete set of photometric data of both targets. The TOI-4479 dataset is composed of 31 transits (22 TESS transits, one MuSCAT2 transit observed simultaneously in g, r, i, and z_s bands, one MuSCAT3 transit observed simultaneously in g_p, R_p, i_p, and z_s bands, and one SINISTRO transit in the i_p band). The TOI-2081 dataset is composed of 26 transits in total (22 TESS transits and one MuSCAT2 transit observed simultaneously in g, r, i, z_s bands). In our calculations, we adopted the values for the stellar parameters shown in Table 1, which were derived from the analysis of ALFOSC spectra.

5.2. Contamination analysis

The possible multiplicity of the system and the subsequent presence of an unresolved companion entails a flux contamination of the host star that may affect the observed transit depth and lead to erroneous parameters of the planetary system (Daemgen et al. 2009). Single-passband photometry is not able to constrain such contamination because of the degeneracy with orbital geometry, limb darkening and planet-to-star radius ratio. Nevertheless, as described in Parviainen et al. (2019), some effects of the flux contamination are color-dependent (Rosenblatt 1971; Drake 2003; Tingley 2004), making multicolor photometry a valuable tool to constrain the degree of contamination and estimate the true planet-to-star radius ratio. On the one hand, color differences between the host star and the companion may lead to significant variations in the transit depth in different passbands. On the other hand, the transiting object produces a color-dependent signal, leaving a distinctive signature that relies either on the radius of the transiting object and the nature of the transiting object. Both effects allow us to determine whether a transiting planet candidate is actually a planet or, conversely, a mimicked signal by flux contamination.

Our multicolor transit analysis pipeline accounts for the effects of flux contamination and estimates, among the system

[3] The TESS SPOC Presearch Data Conditioning Simple Aperture Photometry (PDCDAP; Stumpe et al. 2012, 2014; Smith et al. 2012) light curves.

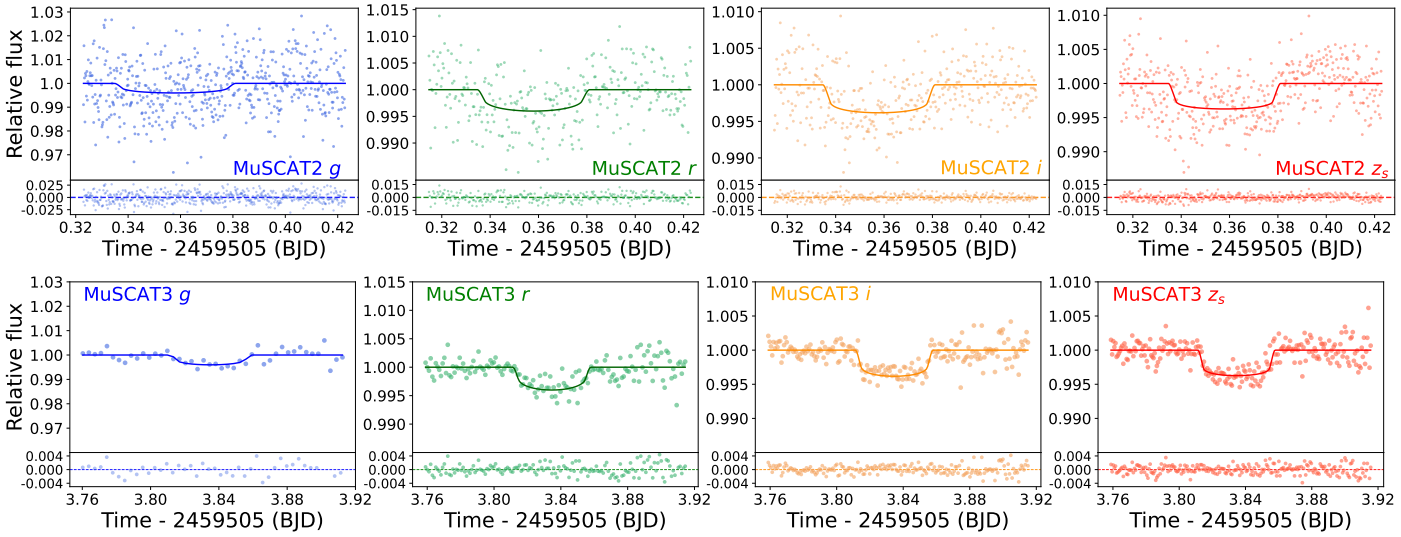

Fig. 5. MuSCAT2 (*top*) and MUSCAT3 (*bottom*) detrended light curves of TOI-4479b in g, r, i, and z_s passbands. The dots show the MuSCAT2 and MUSCAT3 relative flux and the lines show the best light-curve model from the MuSCAT2 pipeline for each band.

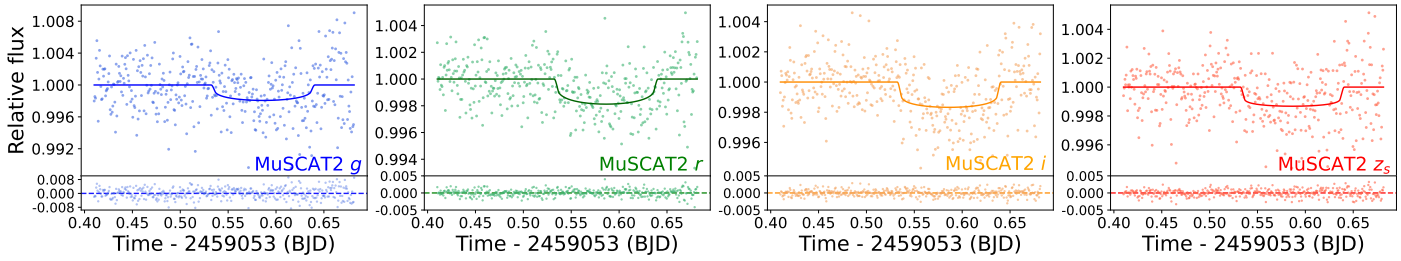

Fig. 6. MuSCAT2 detrended light curves of TOI-2081b in g, r, i, and z_s passbands. The dots show the MuSCAT2 relative flux and the lines show the best light-curve model.

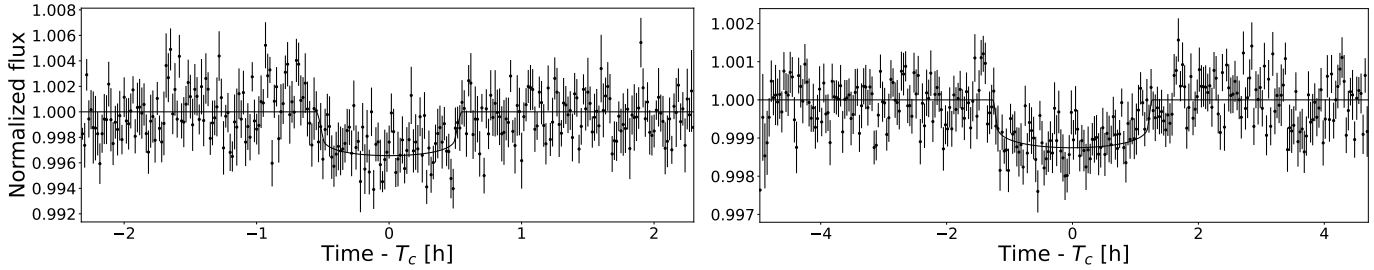

Fig. 7. TESS PDCSAP folded relative flux from the combination of all the transits and best light-curve model of TOI-4479b (*left*) and TOI-2081b (*right*).

parameters, the posterior distributions of the apparent radius ratio, the true radius ratio (free of the contribution of the contaminant), and the effective temperature of the possible contaminant companion. By analyzing these three parameters, we are able to evaluate the flux contamination and to validate the nature of the companion.

6. Results and discussion

In this section, we validate the planetary nature and discuss the properties of TOI-2081b and TOI-4479b. We evaluate the possible flux contamination in both systems by studying the posterior distributions of the true and apparent planet-to-star radius ratio ($k_{\rm true}$, $k_{\rm app}$) and the difference in effective temperature between the possible contaminant and the host star ($\Delta T_{\rm eff}$) parameters.

6.1. TOI-4479

We show the phase-folded combined MuSCAT2, TESS, and SINISTRO photometric datasets of TOI-4479b with the best light-curve models in Figs. 5, 7, and 8, respectively. Also, in Table 2 we show the derived stellar and planetary parameters from our multicolor validation pipeline. The corner plot showing the parameter posterior distributions can be found in Fig. A.2.

To evaluate the possible flux contamination, in Fig. 9 we show the posterior distribution of the true radius ratio ($k_{\rm true}$) as a function of the difference in effective temperature between the contaminant and the host star ($\Delta T_{\rm eff}$), the apparent radius ratio ($k_{\rm app}$), the impact parameter, and the stellar density. We also show a comparison among the posterior distributions of the apparent and true radius ratio as well as the effective

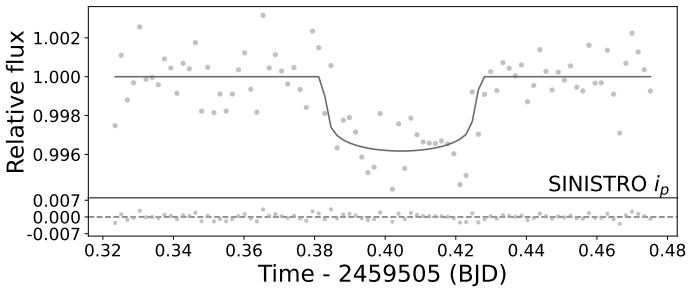

Fig. 8. SINISTRO detrended light-curve of TOI-4479b in the i_p passband. The dots show the SINISTRO relative flux and the line shows the best light-curve model.

Table 2. Planetary parameters of TOI-2081b and TOI-4479b derived through the multicolor validation pipeline.

	TOI-4479b	TOI-2081b
R_p [$R_\oplus$]	$2.82^{+0.65}_{-0.63}$	$2.04^{+0.50}_{-0.54}$
$k_{\rm app}$	$0.0572^{+0.0024}_{-0.0017}$	$0.0350^{+0.0032}_{-0.0041}$
$k_{\rm true}$	$0.062^{+0.011}_{-0.004}$	$0.0396^{+0.0039}_{-0.0024}$
$P_{\rm orb}$ [days]	$1.15890^{+0.00001}_{-0.00002}$	$10.50534^{+0.00007}_{-0.00008}$
a/R_*	$7.8^{+0.7}_{-1.4}$	$30.3^{+1.9}_{-4.8}$
a [AU]	$0.0164^{+0.0015}_{-0.0029}$	$0.0752^{+0.0047}_{-0.0119}$
b	$0.43^{+0.24}_{-0.30}$	$0.35^{+0.27}_{-0.24}$
i [deg]	$86.36^{+2.49}_{-2.72}$	$89.34^{+0.46}_{-0.73}$
$T_{\rm c}$ [BJD]	$2459420.7578^{+0.0013}_{-0.0011}$	$2458685.8996^{+0.0029}_{-0.0028}$
$T_{\rm eq}$ [K]	861^{+64}_{-103}	488^{+28}_{-52}
M_p [$M_\oplus$] (1)	$8.3^{+8.0}_{-4.1}$	$5.0^{+4.8}_{-2.4}$
F [$F_\oplus$]	$92.5^{+17.5}_{-33.3}$	$8.1^{+1.1}_{-2.6}$
K [m s^{-1}] (2,3)	7.12	1.72

Notes. (1)Predicted masses using `Forecaster` (Chen & Kipping 2017) empirical mass-radius relation. (2)Taken from the TESS Input Catalog (`TICv8`, Stassun et al. 2019). (3)Predicted RV semiamplitude.

temperatures of the host star and contaminant for the TOI-4479 system in Fig. 10.

For TOI-4479, we found $k_{\rm true}$ to be close in value to $k_{\rm app}$ (Fig. 9), implying a very low degree of flux contamination from a possible companion. Thus, considering the contamination negligible, we derived the size of the companion from the $k_{\rm app}$, leading to a $2.82^{+0.65}_{-0.63}$ $R_\oplus$ sized object. Moreover, the posterior distribution of $\Delta T_{\rm eff}$ is centered around 0, meaning that the effective temperature of the possible contaminant would be the same as that of the host star, and the posterior distribution of the impact parameter implies a non-grazing transit. Thus, we can validate TOI-4479b as a sub-Neptune-sized planet orbiting an M dwarf with a period of $1.15890^{+0.00001}_{-0.00002}$ days.

In Fig. 11, we compare TOI-4479b with the sample of confirmed planets around M dwarfs known to date in the period-radius plane. We also compare TOI-4479b with the entire population of confirmed planets with a radius uncertainty below 10%, showing that TOI-4479b lies in an underpopulated region of the period-radius plane known as the Neptune desert. This deserted region contrasts with the highly populated regions of hot-Jupiters ($R_{\rm p} > 10\ R_\oplus$) and ultra-short-period (USP) rocky planets ($R_{\rm p} < 2\ R_\oplus$) located above and below the Neptune desert, respectively. In Fig. 11, we plot the lower and upper boundaries among these regions as derived by Mazeh et al. (2016) with dashed-dotted lines. The dearth of short-period Neptune-sized planets has been widely studied in the literature and several formation mechanisms (e.g., photo-evaporation, high-eccentricity migration, and in situ formation) have been considered to explain the causes of the Neptune desert region (Sanchis-Ojeda et al. 2014; Mazeh et al. 2016; Lundkvist et al. 2016; Lopez 2017; Owen & Wu 2017; Owen & Lai 2018).

Although TOI-4479b has a slightly longer period that the common definition of USP planets ($P_{\rm orb} < 1$ day), given their shared properties we associate it here to this population. TOI-4479b joins a small group of known USP intermediate-sized planets inhabiting the Neptune desert, namely LTT 9779b (Jenkins et al. 2020), LP 714-47 b (Dreizler et al. 2020), HATS-37Ab (Jordán et al. 2020), HATS-38b (Jordán et al. 2020), TOI-824 b (Burt et al. 2020), TOI-849 b (Armstrong et al. 2020), TOI-132 b (Díaz et al. 2020), and TOI-674 b (Murgas et al. 2021). The existence of such uncommon planets has been interpreted as a consequence of the photo-evaporation produced over short timescales by the strong stellar irradiation experienced by some low-mass planets, which are unable to retain the H/He envelope (Jenkins et al. 2020). However, TOI-4479b is among the biggest USP planets in the desert, meaning that it still retains an appreciable fraction of its volatile envelope in an early stage of the stripping process. We find TOI-4479b to be the biggest USP planet orbiting an M dwarf known to date. We used `Forecaster`[4] (Chen & Kipping 2017) to predict the plausible mass of TOI-4479b, which is $M_{\rm p} = 8.3^{+8.0}_{-4.1}\ M_\oplus$. We note that the error bars on the mass are dominated by the intrinsic spread of the mass-radius distribution for Neptunian planets relatively to the simple power-law relation. We evaluated the prospects to spectroscopically investigate the atmosphere of TOI-4479b by computing the transmission spectroscopy metric (TSM), as defined by Kempton et al. (2018). The TSM is inversely proportional to the planetary mass, and using the forecasted mass range the TSM ranges between 26 and 198 with a peak at TSM $\sim$ 75. According to Kempton et al. (2018), Neptune-sized planets with TSM $\gtrsim$ 90 are the highest-priority candidates for transmission spectroscopy with the JWST, where the ranking is based on the predicted signal-to-noise (S/N) of atmospheric detections. However, individual planets with TSM < 90 can still be extremely suitable candidates for transmission spectroscopy with the JWST, based on scientific merit. This applies to TOI-4479b due to the fact that it orbits an M star and is located in the Neptune desert.

6.2. TOI-2081

We show the phase-folded combined MuSCAT2 and TESS photometric datasets of TOI-2081b together with the best light-curve models in Figs. 6 and 7, respectively. Also, in Table 2 we show the derived stellar and planetary parameters from our multicolor validation pipeline. The corner-plot showing the parameter posterior distributions can be found in Fig. A.3.

To evaluate the possible flux contamination, in Fig. 9 we show the posterior distribution $k_{\rm true}$ as a function of the difference in $\Delta T_{\rm eff}$, $k_{\rm app}$, the impact parameter and the stellar density. The comparison among the posterior distributions of the

[4] https://github.com/chenjj2/forecaster

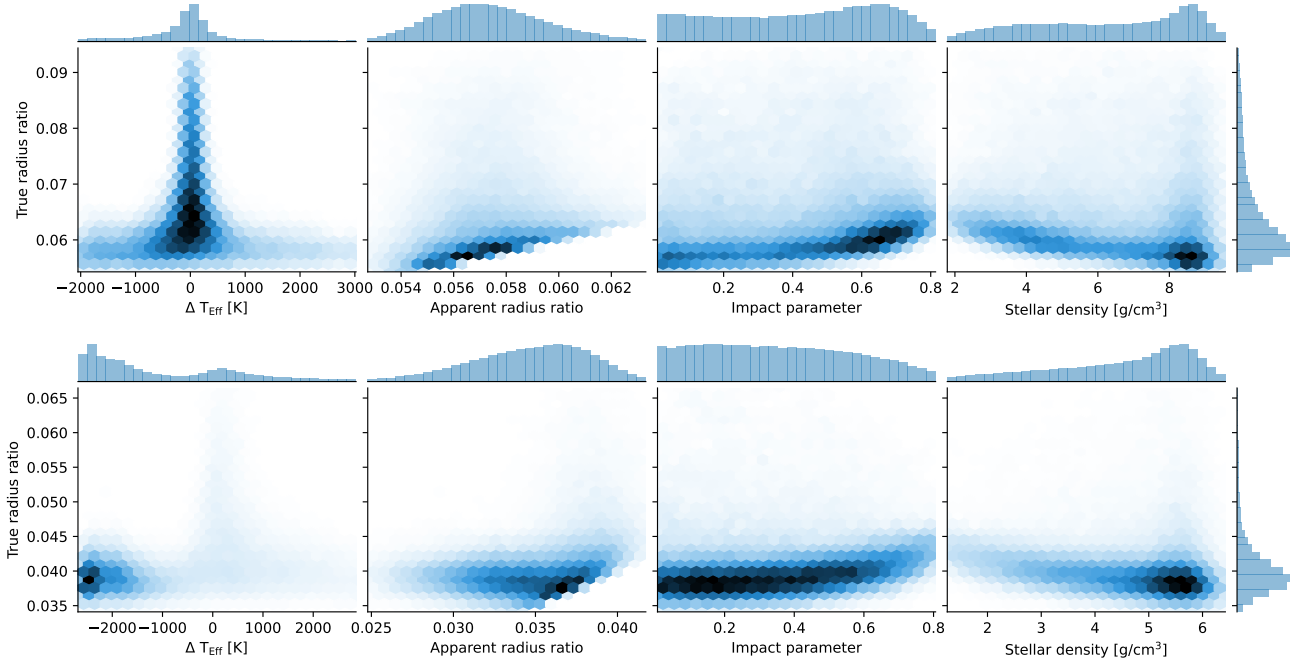

Fig. 9. *From left to right*, posterior distributions of $k_{\rm true}$ versus $\Delta T_{\rm eff}$, $k_{\rm app}$, the impact parameter, and the stellar density from the joint multicolor light-curve analysis, for TOI-4479 (*top four panels*) and TOI-2081 (*bottom four panels*).

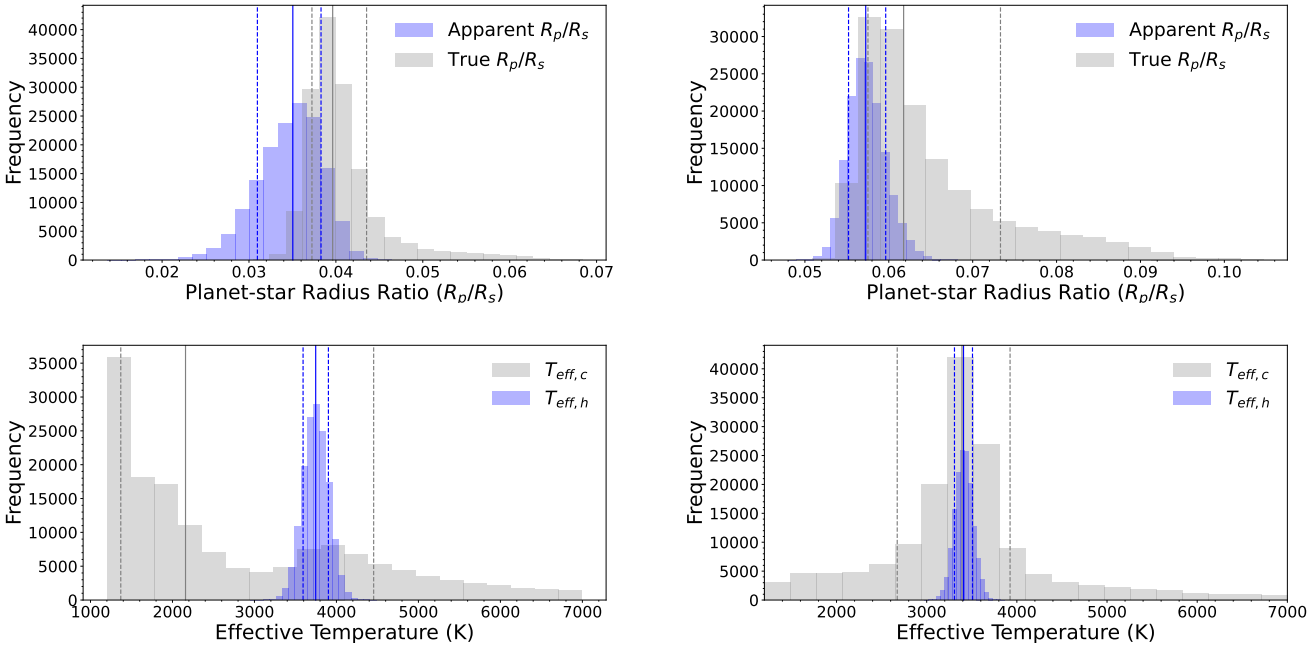

Fig. 10. Comparison among the posterior distributions of the apparent and true radius ratio and the effective temperatures of the host star and contaminant. *Upper panels*: posterior distributions of the true radius ratio ($k_{\rm true}$) and the apparent radius ratio ($k_{\rm app}$) for TOI-2081 (*left*) and TOI-4479 systems (*right*). *Lower panels*: posterior distributions of the effective temperature of the host star ($T_{\rm eff,\,h}$) and the effective temperature of the contaminant ($T_{\rm eff,\,c}$) for TOI-2081 (*left*) and TOI-4479 systems (*right*). The solid lines show the median of each distribution and the dashed lines show the lower and upper 1σ.

apparent and true radius ratio as well as the effective temperatures of the host star and contaminant for TOI-2081 system is shown in Fig. 10.

For TOI-2081, we found $k_{\rm true}$ to be close in value to $k_{\rm app}$ (Fig. 9), implying a very low degree of flux contamination from the companion. Considering the contamination negligible, we derived the size of the companion from the $k_{\rm app}$, leading to a $2.04^{+0.49}_{-0.54}$ $R_\oplus$ sized object. Thus, we can validate TOI-2081b as a super-Earth-sized planet orbiting an M dwarf with a period of $10.50534^{+0.00007}_{-0.00008}$ days.

TOI-2081b is also included in the radius-period diagram in Fig. 11. We find TOI-2081b to be a temperate super-Earth, in a well-populated parameter space region both around M dwarfs and earlier stellar-type hosts.

TOI-2081b ($a \sim 0.07$ AU) is orbiting within the inner edge of the habitable zone of its star (we find a conservative

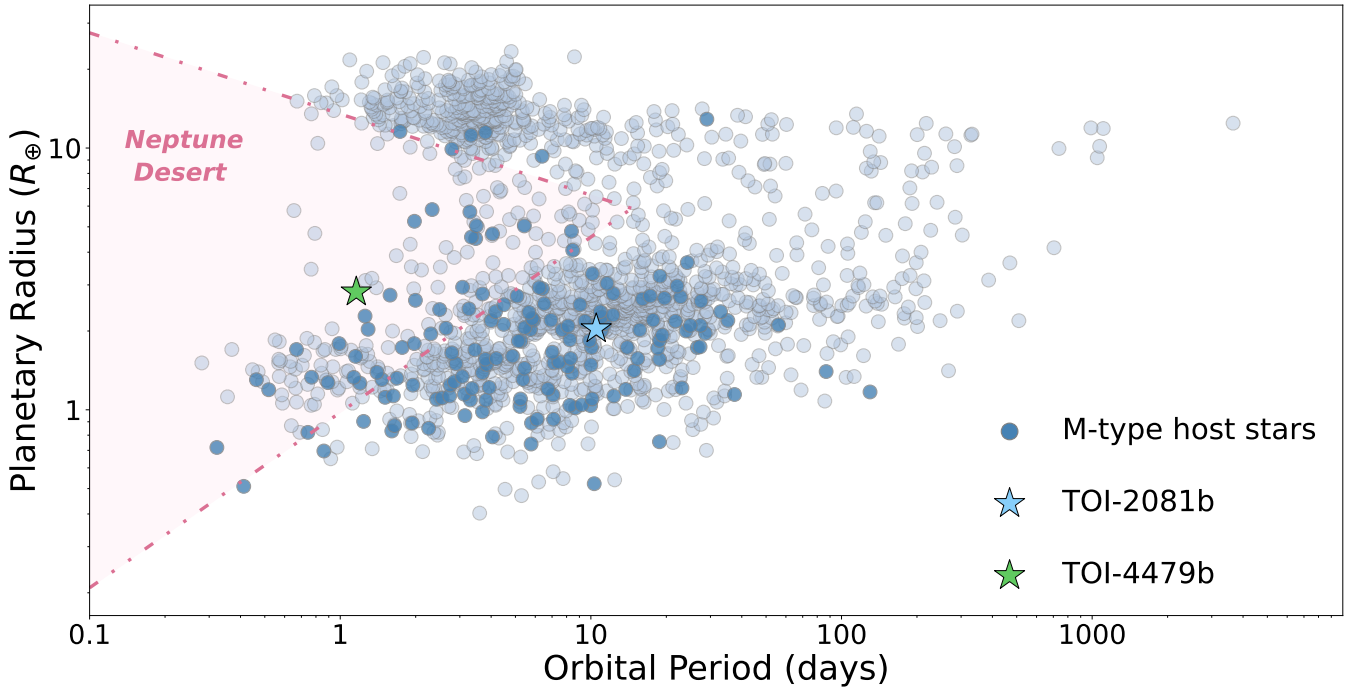

Fig. 11. TOI-4479b and TOI-2081b in the period-radius diagram compared to all the confirmed planets to date with a radius uncertainty below 10%. The dark blue dots show the planets around M-type stars and the dashed-dotted lines show the Neptune desert boundaries in the period-radius plane derived by Mazeh et al. (2016).

habitable zone of $[0.16 \pm 0.02, 0.34 \pm 0.04]$ AU) and in a tidally locked regime. Assuming a zero Albedo and a cloud-free atmosphere without greenhouse gases, the temperature of the day side is estimated at around $T_{\rm day} \approx 680$K. Using `Forecaster`, we estimated a mass of $M_{\rm p} = 5.0^{+4.8}_{-2.4}\,M_\oplus$. The corresponding TSM ranges between 14 and 89 with peak at TSM $\sim$ 35.

7. Conclusions

By using multicolor photometric observations with MuSCAT2, MuSCAT3, and LCOGT 1m, we determined that the degree of contamination by a possible nearby contaminant is negligible in both the TOI-4479b and the TOI-2081b systems, and validated their planetary nature. TOI-4479b is a sub-Neptune-sized planet ($R_{\rm p} = 2.82^{+0.65}_{-0.63}\,R_\oplus$) and TOI-2081b is a super-Earth-sized planet ($R_{\rm p} = 2.04^{+0.49}_{-0.54}\,R_\oplus$). Both planets orbit around M dwarf host stars with orbital periods of 10.50534 ± 0.00007 days and $1.15890^{+0.00002}_{-0.00001}$ days, respectively.

We also found that the TOI-4479b lies in the Neptune desert and joins a small sample of ($\sim$8) short-period, intermediate-sized planets, with TOI-4479b being the biggest USP planet orbiting an M dwarf known to date. Thus, this planet is an interesting target for future radial velocity observations (which will require very large telescope apertures) and atmospheric studies, as its full characterization may provide significant observational constraints for planet formation and evolution theories.

Acknowledgements. We thank the anonymous referee for insightful suggestions, which added the clarity of this paper. Funding for the TESS mission is provided by NASA's Science Mission Directorate. We acknowledge the use of public TESS data from pipelines at the TESS Science Office and at the TESS Science Processing Operations Center. Resources supporting this work were provided by the NASA High-End Computing (HEC) Program through the NASA Advanced Supercomputing (NAS) Division at Ames Research Center for the production of the SPOC data products. We acknowledge the use of public TESS data from pipelines at the TESS Science Office and at the TESS Science Processing Operations Center. This research has made use of the Exoplanet Follow-up Observation Program website, which is operated by the California Institute of Technology, under contract with the National Aeronautics and Space Administration under the Exoplanet Exploration Program. This paper includes data collected by the TESS mission that are publicly available from the Mikulski Archive for Space Telescopes (MAST). This paper is based on observations made with the MuSCAT2 instrument, developed by ABC, at Telescopio Carlos Sánchez operated on the island of Tenerife by the IAC in the Spanish Observatorio del Teide. This paper is based on observations made with the MuSCAT3 instrument, developed by the Astrobiology Center and under financial supports by JSPS KAKENHI (JP18H05439) and JST PRESTO (JPMJPR1775), at Faulkes Telescope North on Maui, HI, operated by the Las Cumbres Observatory. This work makes use of observations from the LCOGT network. Part of the LCOGT telescope time was granted by NOIRLab through the Mid-Scale Innovations Program (MSIP). MSIP is funded by NSF. Based on observations made with the Nordic Optical Telescope, owned in collaboration by the University of Turku and Aarhus University, and operated jointly by Aarhus University, the University of Turku and the University of Oslo, representing Denmark, Finland and Norway, the University of Iceland and Stockholm University at the Observatorio del Roque de los Muchachos, La Palma, Spain, of the Instituto de Astrofisica de Canarias. The data presented here were obtained in part with ALFOSC, which is provided by the Instituto de Astrofisica de Andalucia (IAA) under a joint agreement with the University of Copenhagen and NOT. This work made use of `tpfplotter` by J. Lillo-Box (publicly available in `www.github.com/jlillo/tpfplotter`), which also made use of the python packages `astropy`, `lightkurve`, `matplotlib` and `numpy`. E.E.-B. acknowledges financial support from the European Union and the State Agency of Investigation of the Spanish Ministry of Science and Innovation (MICINN) under the grant PRE2020-093107 of the Pre-Doc Program for the Training of Doctors (FPI-SO) through FSE funds. G.M. has received funding from the European Union's Horizon 2020 research and innovation programme under the Marie Skłodowska-Curie grant agreement No. 895525. C.D.D. acknowledges support provided by the NASA Exoplanets Research Program (XRP) via grant 80NSSC20K0250. J.K. gratefully acknowledge the support of the Swedish National Space Agency (SNSA; DNR 2020-00104). R.L. acknowledges financial support from the Spanish Ministerio de Ciencia e Innovación, through project PID2019-109522GB-C52, and the Centre of Excellence "Severo Ochoa" award to the Instituto de Astrofísica de Andalucía (SEV-2017-0709). A.A.B. and M.V.G. acknowledge the support of Ministry of Science and Higher Education of the Russian Federation under the grant 075-15-2020-780(N13.1902.21.0039). M.T. is supported by JSPS KAKENHI grant Nos.18H05442, 15H02063, and 22000005. M.R.Z.O. acknowledges

financial support from the Spanish Ministerio de Ciencia e Innovación through project PID2019-109522GB-C51. This work is partly supported by JSPS KAKENHI Grant Numbers 22000005, JP15H02063, JP17H04574, JP18H05439, P18H05442, JP20K14518, JP20K14521, JP21K13975, JP21K20376, Grant-in-Aid for JSPS Fellows Grant Number JP20J21872, JST CREST Grant Number JPMJCR1761, and the Astrobiology Center of National Institutes of Natural Sciences (NINS) (Grant Numbers AB022006, AB031010, AB031014).

References

Allard, F., Homeier, D., & Freytag, B. 2012, Phil. Trans. R. Soc. London Ser. A, 370, 2765
Aller, A., Lillo-Box, J., Jones, D., Miranda, L. F., & Barceló Forteza, S. 2020, A&A, 635, A128
Armstrong, D. J., Lopez, T. A., Adibekyan, V., et al. 2020, Nature, 583, 39
Brown, T. M., Baliber, N., Bianco, F. B., et al. 2013, PASP, 125, 1031
Burt, J. A., Nielsen, L. D., Quinn, S. N., et al. 2020, AJ, 160, 153
Cameron, A. C. 2012, Nature, 492, 48
Chen, J., & Kipping, D. 2017, ApJ, 834, 17
Ciardi, D. R., Beichman, C. A., Horch, E. P., & Howell, S. B. 2015, ApJ, 805, 16
Cifuentes, C., Caballero, J. A., Cortés-Contreras, M., et al. 2020, A&A, 642, A115
Collins, K. A., Kielkopf, J. F., Stassun, K. G., & Hessman, F. V. 2017, AJ, 153, 77
Daemgen, S., Hormuth, F., Brandner, W., et al. 2009, A&A, 498, 567
Díaz, M. R., Jenkins, J. S., Gandolfi, D., et al. 2020, MNRAS, 493, 973
Drake, A. J. 2003, ApJ, 589, 1020
Dreizler, S., Crossfield, I. J. M., Kossakowski, D., et al. 2020, A&A, 644, A127
Foreman-Mackey, D., Hogg, D. W., Lang, D., & Goodman, J. 2013, PASP, 125, 306
Fukui, A., Kimura, T., Hirano, T., et al. 2022, PASJ, 74, L1
Gaia Collaboration (Brown, A. G. A., et al.) 2018, A&A, 616, A1
Gaia Collaboration (Brown, A. G. A., et al.) 2021, A&A, 649, A1
Gavel, D., Kupke, R., Dillon, D., et al. 2014, SPIE, 9148, 914805
Guerrero, N. M., Seager, S., Huang, C. X., et al. 2021, ApJS, 254, 39
Husser, T. O., Wende-von Berg, S., Dreizler, S., et al. 2013, A&A, 553, A6
Jenkins, J. M. 2002, ApJ, 575, 493
Jenkins, J. M., Chandrasekaran, H., McCauliff, S. D., et al. 2010, SPIE Conf. Ser., 7740, 77400D
Jenkins, J. M., Twicken, J. D., McCauliff, S., et al. 2016, SPIE Conf. Ser., 9913, 99133E
Jenkins, J. S., Díaz, M. R., Kurtovic, N. T., et al. 2020, Nat. Astron., 4, 1148
Jensen, E. 2013, Astrophysics Source Code Library [record ascl:1306.007]
Jordán, A., Bakos, G. Á., Bayliss, D., et al. 2020, AJ, 160, 222
Kempton, E. M. R., Bean, J. L., Louie, D. R., et al. 2018, PASP, 130, 114401
Kesseli, A. Y., West, A. A., Veyette, M., et al. 2017, ApJS, 230, 16
Kupke, R., Gavel, D., Roskosi, C., et al. 2012, SPIE Conf. Ser., 8447, 84473G
Li, J., Tenenbaum, P., Twicken, J. D., et al. 2019, PASP, 131, 024506
Lopez, E. D. 2017, MNRAS, 472, 245
Lundkvist, M. S., Kjeldsen, H., Albrecht, S., et al. 2016, Nat. Commun., 7, 11201
Mazeh, T., Holczer, T., & Faigler, S. 2016, A&A, 589, A75
McCully, C., Volgenau, N. H., Harbeck, D.-R., et al. 2018, SPIE Conf. Ser., 10707, 107070K
McGurk, R., Rockosi, C., Gavel, D., et al. 2014, SPIE Conf. Ser., 9148, 91483A
Murgas, F., Astudillo-Defru, N., Bonfils, X., et al. 2021, A&A, 653, A60
Narita, N., Fukui, A., Kusakabe, N., et al. 2019, J. Astron. Teles. Instrum. Syst., 5, 015001
Narita, N., Fukui, A., Yamamuro, T., et al. 2020, SPIE Conf. Ser., 11447, 114475K
Oke, J. B. 1990, AJ, 99, 1621
Owen, J. E., & Lai, D. 2018, MNRAS, 479, 5012
Owen, J. E., & Wu, Y. 2017, ApJ, 847, 29
Parviainen, H. 2015, MNRAS, 450, 3233
Parviainen, H. 2018, in Handbook of Exoplanets, ed. H. J. Deeg, & J. A. Belmonte (Berlin: Springer), 149
Parviainen, H., & Aigrain, S. 2015, MNRAS, 453, 3821
Parviainen, H., Tingley, B., Deeg, H. J., et al. 2019, A&A, 630, A89
Parviainen, H., Palle, E., Zapatero-Osorio, M. R., et al. 2020, A&A, 633, A28
Parviainen, H., Palle, E., Zapatero-Osorio, M. R., et al. 2021, A&A, 645, A16
Ricker, G. R., Winn, J. N., Vanderspek, R., et al. 2015, J. Astron. Teles. Instrum. Syst., 1, 014003
Rosenblatt, F. 1971, Icarus, 14, 71
Safonov, B. S., Lysenko, P. A., & Dodin, A. V. 2017, Astron. Lett., 43, 344
Sanchis-Ojeda, R., Rappaport, S., Winn, J. N., et al. 2014, ApJ, 787, 47
Savel, A. B., Dressing, C. D., Hirsch, L. A., et al. 2020, AJ, 160, 287
Skrutskie, M. F., Cutri, R. M., Stiening, R., et al. 2006, AJ, 131, 1163
Smith, J. C., Stumpe, M. C., Van Cleve, J. E., et al. 2012, PASP, 124, 1000
Stassun, K. G., Oelkers, R. J., Paegert, M., et al. 2019, AJ, 158, 138
Stumpe, M. C., Smith, J. C., Van Cleve, J. E., et al. 2012, PASP, 124, 985
Stumpe, M. C., Smith, J. C., Catanzarite, J. H., et al. 2014, PASP, 126, 100
Tingley, B. 2004, A&A, 425, 1125
Tody, D. 1993, ASP Conf. Ser., 52, 173
Twicken, J. D., Catanzarite, J. H., Clarke, B. D., et al. 2018, PASP, 130, 064502
Wright, E. L., Eisenhardt, P. R. M., Mainzer, A. K., et al. 2010, AJ, 140, 1868

[1] Instituto de Astrofísica de Canarias (IAC), 38200 La Laguna, Tenerife, Spain
e-mail: emma.esparza.borges@iac.es
[2] Departamento de Astrofísica, Universidad de La Laguna (ULL), 38206 La Laguna, Tenerife, Spain
[3] Department for Physics and Astronomy, University of Heidelberg, Germany
[4] Landesternwarte Königstuhl (LSW), Zentrum für Astronomie der Universität Heidelberg, Königstuhl 12, 69117 Heidelberg, Germany
[5] Centro de Astrobiologia (CSIC-INTA), Carretera de Ajalvir km 4, 28850 Torrejon de Ardoz, Madrid, Spain
[6] Leiden Observatory, Leiden University, Postbus 9513, 2300 RA, Leiden, The Netherlands
[7] Center for Astrophysics, Harvard & Smithsonian, 60 Garden Street, Cambridge, MA 02138, USA
[8] Department of Astronomy, University of California Berkeley, Berkeley, CA 94720, USA
[9] Department of Astronomy, University of Maryland, College Park, College Park, MD 20742 USA
[10] Department of Space, Earth and Environment, Astronomy and Plasma Physics, Chalmers University of Technology, 412 96 Gothenburg, Sweden
[11] Instituto de Astrofísica de Andalucía (IAA-CSIC), Glorieta de la Astronomía s/n, 18008 Granada, Spain
[12] Sternberg Astronomical Institute, Lomonosov Moscow State University, 13 Universitetski prospekt, 119992 Moscow, Russia University, Russia
[13] Astrobiology Research Unit, Université de Liège, 19C Allée du 6 Août, 4000 Liège, Belgium
[14] Patashnick Voorheesville Observatory, Voorheesville, NY 12186, USA
[15] Department of Physics, Massachusetts Institute of Technology, Cambridge, MA 02139, USA
[16] MIT Kavli Institute for Astrophysics and Space Research, Cambridge, MA 02139, USA
[17] Komaba Institute for Science, The University of Tokyo, 3-8-1 Komaba, Meguro, Tokyo 153-8902, Japan
[18] Astrobiology Center, 2-21-1 Osawa, Mitaka, Tokyo 181-8588, Japan
[19] Department of Astronomy, The University of Tokyo, 7-3-1, Hongo, Bunkyo-ku, Tokyo 113-0033, Japan
[20] National Astronomical Observatory of Japan, 2-21-1 Osawa,Mitaka, Tokyo 181-8588, Japan
[21] Division of Science, National Astronomical Observatory of Japan, 2-21-1 Osawa, Mitaka, Tokyo 181-8588, Japan
[22] SETI Institute, Mountain View, CA 94043, USA
[23] NASA Ames Research Center, Moffett Field, CA 94035, USA
[24] Department of Multi-Disciplinary Sciences, Graduate School of Arts and Sciences, The University of Tokyo, 3-8-1 Komaba, Meguro, Tokyo 153-8902, Japan
[25] Institute of Astronomy and Astrophysics, Academia Sinica, PO Box 23-141, Taipei 10617, Taiwan, R.O.C.
[26] Department of Astrophysics, National Taiwan University, Taipei 10617, Taiwan, R.O.C.
[27] Department of Aeronautics and Astronautics, Massachusetts Institute of Technology, Cambridge, MA 02139, USA
[28] Department of Earth, Atmospheric, and Planetary Sciences, Massachusetts Institute of Technology, 77 Massachusetts Avenue, Cambridge, MA 02139, USA
[29] Department of Astrophysical Sciences, Princeton University, Princeton, NJ 08544, USA

Appendix A: Additional plots

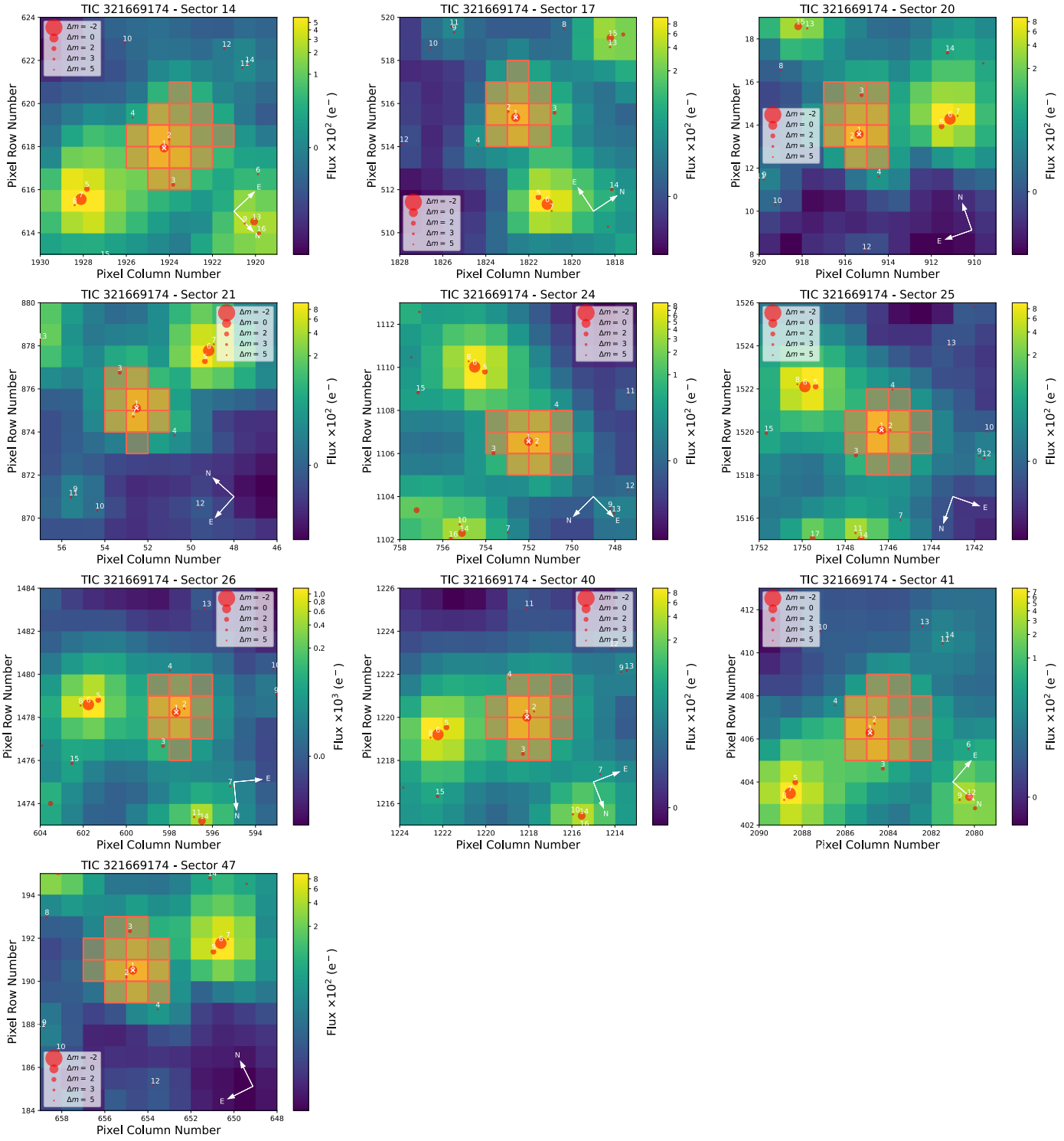

Fig. A.1. TESS target pixel file images of TOI-2081 observed in Sectors 14, 17, 20, 21, 24, 25, 26, 40, 41, and 47. The red circles show the sources in the field identified by the *Gaia DR2* catalogue with scaled magnitudes. The position of the targets is indicated by white crosses and the mosaic of orange squares show the mask used by the pipeline to extract photometry. These plots were made using `tpfplotter` (Aller et al. 2020).

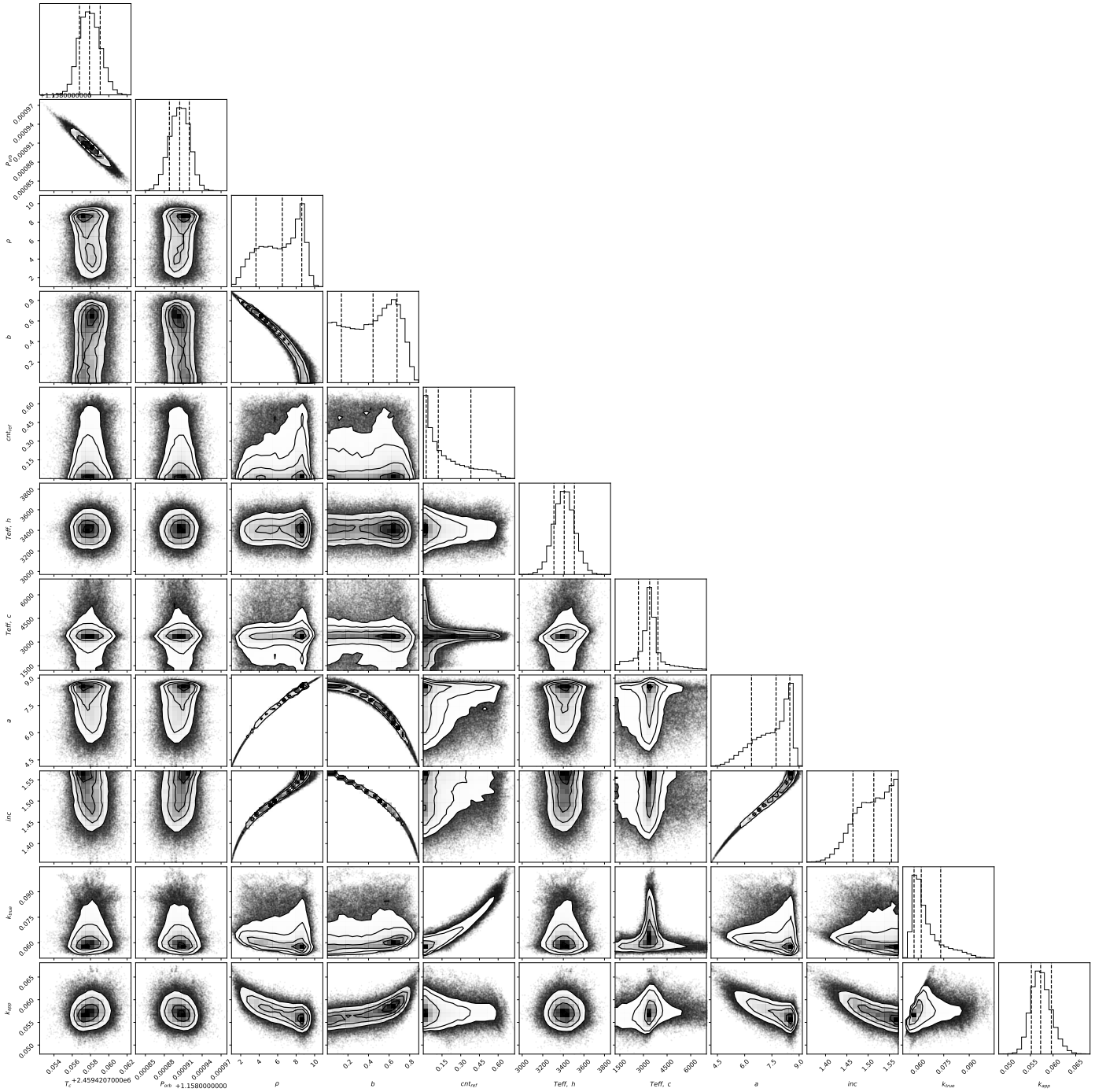

Fig. A.2. Corner plot of the posterior distributions obtained through the multicolor validation pipeline for TOI-4479.

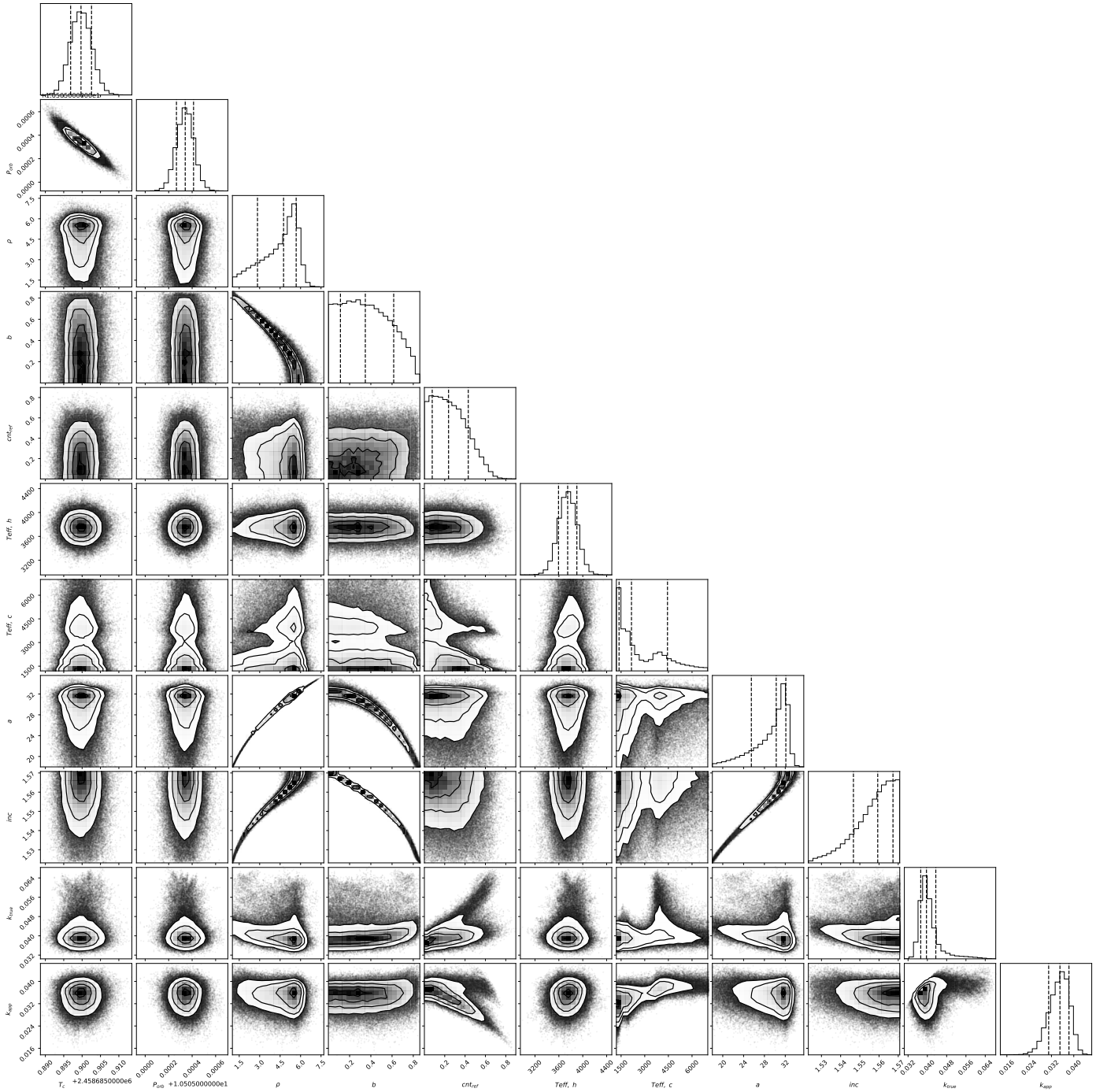

Fig. A.3. Corner plot of the posterior distributions obtained through the multicolor validation pipeline for TOI-2081.